Large−Eddy Simulation of Turbulent Flux Patterns over Oasis Surface

Bangjun Cao[1,2], Yaping Shao[2], Xianyu Yang[1,2], Xin Yin[2], Shaofeng Liu[3]

[1]School of Atmospheric Sciences, Chengdu University of Information Technology, Chengdu, 610225, China
[2]Institute for Geophysics and Meteorology, University of Cologne, Cologne, 50923, Germany
[3]Southern Marine Science and Engineering Guangdong Laboratory (Zhuhai), School of Atmospheric Sciences, Sun Yat-sen University, Zhuhai, China.

Correspondence to: Xianyu Yang (xyang@cuit.edu.cn)

Abstract. Large-eddy simulation (LES) has been increasingly used for studying atmosphere and land surface interactions over heterogeneous areas. However, the parameterizations based on the Monin-Obukhov Similarity Theory (MOST) often violate the basic assumptions of the very theory, generate inconsistencies with the LES turbulence closures, and produce surface flux estimates dependent on LES-model resolution. Here, we propose a novel scheme for turbulent flux estimates in LES models. It computes the fluxes locally using the LES subgrid closure, which is then constrained on the macroscopic scale using the MOST. Compared with several other schemes, the new scheme performs better for the various types of land surfaces tested. We further validate our scheme by comparing surface flux estimates with field measurements obtained over an oasis surface at various height levels. Additionally, we scrutinize other quantities related to surface energy balance, including net radiation, ground heat flux, and surface skin temperature, all of which align well with observational data. Our sensitivity experiments, focusing on horizontal resolution, underscore the robustness of our scheme, as it maintains its corrective efficacy despite changes in horizontal grid spacing. We find that the macroscopic constraint imposed by MOST on LES-estimated fluxes strengthens as the horizontal grid spacing decreases, with a more pronounced influence on sensible than latent heat fluxes. These findings collectively highlight the promise and adaptability of our scheme for enhancing surface flux estimations in LES models.

1 Introduction

Surface fluxes characterize the exchanges of energy, mass, and momentum between the surface and atmosphere and serve as the lower boundary conditions for atmospheric model simulations. How to estimate the fluxes is a central task of Land Surface Models (LSMs) (Oleson et al., 2007). In almost all existing LSMs, they are parameterized via a network of aerodynamic resistances estimated using the Monin-Obukhov Similarity Theory (MOST) (Monin and Obukhov, 1954), which assumes the atmospheric boundary layer to be stationary and horizontally homogeneous.

In recent years, large-eddy simulation (LES) models have been developed and become a powerful tool for studying land-surface and atmosphere interactions over homogeneous and heterogeneous areas. In current LES models (e.g., Deardorff,

1978; Moeng, 1984; Sullivan et al., 1994), turbulence is divided into grid-resolved large eddies and subgrid small eddies. The effects of subgrid eddies are represented by subgrid closures (e.g., Smagorinsky, 1963; Deardorff, 1980; Holt and Raman, 1988). Early LES models are not coupled with LSM; instead, land surface forcing is prescribed (e.g., Maronga and Raasch, 2013). In recent years, LES models coupled with LSM have been widely used to study atmospheric turbulence over idealized (e.g., Patton et al., 2005) and natural (e.g., Huang and Margulis, 2010; Shao et al., 2013) heterogeneous surfaces. Estimating surface fluxes for LES models is usually also based on the MOST. However, the near-surface diffusivity and viscosity estimated by the MOST-based schemes often diverge from those derived from LES subgrid closures, causing inconsistencies between them (Redelsperger et al., 2001).

To deal with this inconsistency problem in LES models, a strategy is proposed by Shao et al. (2013) to estimate surface fluxes based on the subgrid closure. This strategy ensures that the surface flux estimates and subgrid closure are on a consistent physical basis. However, this strategy requires an extrapolation of eddy diffusivity and viscosity to the surface and thus local surface parameters (e.g., local roughness length), and it is not clear whether the surface fluxes estimated this way satisfy the MOST on the scale for which the theory works well.

The problem of inconsistency between subgrid closure and the MOST in LES models has been studied by Sullivan et al. (1994). Instead of abandoning the use of the MOST, the latter authors proposed a two-part [a turbulent (large eddy) part and a mean-flow part] SGS eddy-viscosity model to achieve better agreement between LES and MOST similarity forms in the surface layer. In their model, the usual SGS turbulent kinetic energy (TKE) formulation for the SGS eddy viscosity is preserved, but a contribution from the mean flow is explicitly included, and the contributions from the turbulent part are reduced near the surface. Sullivan et al. (1994) reported that their model yielded increased fluctuation amplitudes near the surface and better correspondence with similarity forms in the surface layer. While the two-part eddy viscosity model provides an interesting approach to aligning LES SGS with the MOST, it did not explicitly provide a solution for surface flux estimates in LES models. A questionable assumption of their model is the reduced contribution of the turbulent (large eddy) part and increased contribution of the mean part to the subgrid eddy viscosity near the surface, because this assumption reduces the importance of large eddies, which may arise due to surface heterogeneity and thus does not preserve the flux patterns, although the mean values of the flux (in their case, surface shear stress) may be preserved.

This study presents a novel approach for surface flux calculation for LES models. This approach comprises two components. First, it calculates LES subgrid fluxes using eddy viscosity and diffusivity estimates derived from the LES closure without invoking the MOST while considering local turbulence characteristics. Second, it employs a macroscopic constraint to ensure that fluxes averaged over the LES domain, corresponding to scales suitable for MOST application, align with the MOST principles. This scheme requires only LES simulated variable, effectively addresses the previously mentioned limitations, and ensures that LES flux estimates are independent of model resolution. It facilitates the knowledge transfer from LES to RANS models. To evaluate the performance of the new scheme, we select the "Heihe Watershed Allied Telemetry Experimental Research " (HiWATER, Li et al., 2013) site in Zhangye (38.83-38.92 °N, 100.31-100.42 °E,

1556.00-1559.00 m Above Sea Level (ASL)) as the focal point. Additionally, we examine several other existing schemes for comparative analysis.

2 New Surface Flux Scheme for LES Model

The new scheme, denoted as the MOST-r scheme, is composed of two components. First, surface fluxes are locally
70 estimated, here using the 1.5-order TKE closure (Deardorff, 1980) without invoking the MOST similarity functions in LES. Second, we implement a macroscopic constraint by applying the MOST principles to the LES-simulated fluxes (Fig. 1). For the development and validation of this scheme, we have opted for the Weather Research and Forecast (WRF) LES model. Additionally, we have chosen the 1.5-order TKE closure as the LES subgrid closure.
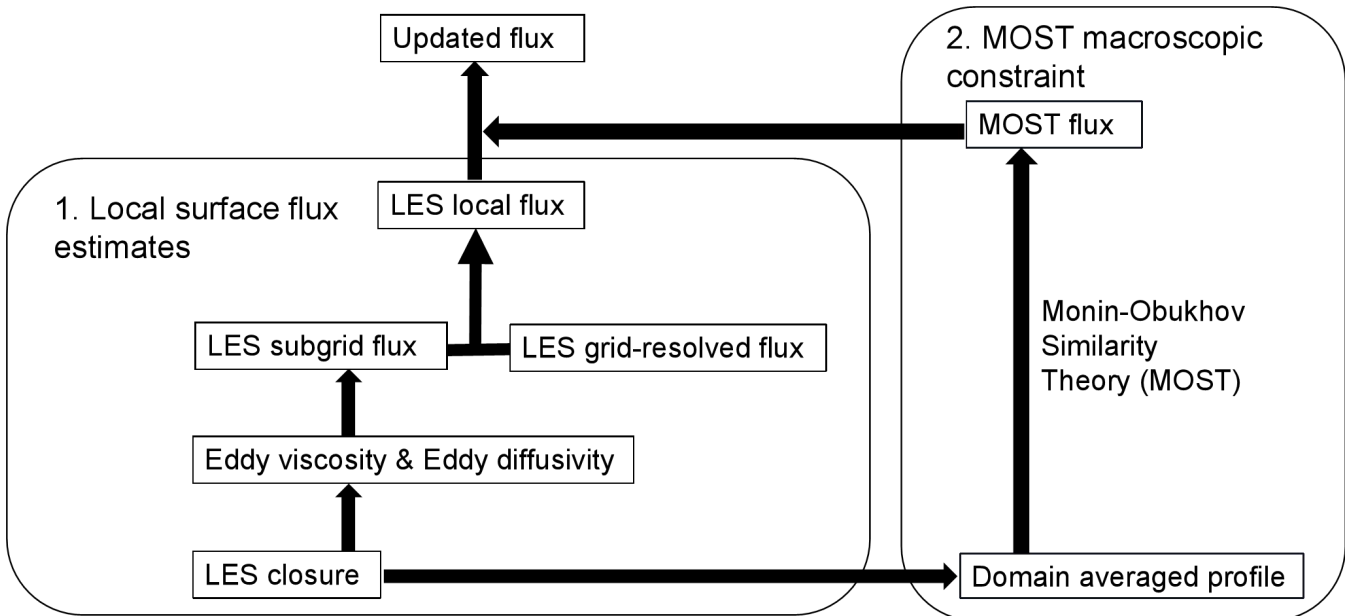
75 **Figure 1.** Schematic diagram of the MOST-r scheme.

2.1 Local surface flux estimates

In LES models, a flux encompasses the contributions from grid-resolved and subgrid eddies, such as sensible and latent heat fluxes, H_{les} and LE_{les},

$$H_{\mathrm{les}} = H_{\mathrm{les,g}} + H_{\mathrm{les,sg}}, \tag{1}$$

80 $$LE_{\mathrm{les}} = LE_{\mathrm{les,g}} + LE_{\mathrm{les,sg}}, \tag{2}$$

where $H_{\mathrm{les,g}}$ and $LE_{\mathrm{les,g}}$ are grid-resolved fluxes derived from the LES-simulated vertical velocity $\widetilde{w}$, temperature $\widetilde{T}$, and specific humidity $\widetilde{q}$, *i.e.*,

$$H_{\mathrm{les,g}} = \rho c_{\mathrm{p}} \widetilde{w} \widetilde{T}, \tag{3}$$

$$LE_{\text{les,g}} = \rho L \widetilde{w}\widetilde{q}, \tag{4}$$

where ρ is air density, L is latent heat coefficient, and c_p is specific heat capacity at constant pressure. At the surface, due to the boundary condition, $\widetilde{w} = 0$, both $H_{\text{les,g}}$ and $E_{\text{les,g}}$ equal zero, and thus $H_{\text{les}} = H_{\text{les,sg}}$ and $LE_{\text{les}} = LE_{\text{les,sg}}$ are conventionally obtained using a LSM, subject to the surface energy and water balance equations, *i.e.*,

$$R_n - H_{\text{les}} - LE_{\text{les}} - G = 0, \tag{5}$$

$$P - E_{\text{les}} - I - R_0 = 0, \tag{6}$$

where R_n is net radiation, G is ground heat flux, P is precipitation, I is infiltration, and R_0 is surface runoff. The subgrid fluxes at the surface are parameterized, typically employing the aerodynamic resistance approach,

$$H_{\text{les,sg}} = -\rho C_p \frac{(\widetilde{T}_a - \widetilde{T}_0)}{r_{\text{h,sg}}}, \tag{7}$$

$$LE_{\text{les,sg}} = -\rho L \beta \frac{(\widetilde{q}_a - q_s(\widetilde{T}_0))}{r_{\text{q,sg}}}, \tag{8}$$

where $\widetilde{T}_a$ and $\widetilde{q}_a$ are air temperature and specific humidity at the lowest model layer, respectively; $\widetilde{T}_0$ is surface temperature and $q_s(\widetilde{T}_0)$ saturation specific humidity at $\widetilde{T}_0$; parameter β can be expressed as a function of the topsoil moisture (e.g., Irannejad and Shao, 1998); and $r_{\text{h,sg}}$ and $r_{\text{q,sg}}$ are aerodynamic resistances for heat and water vapor, respectively, commonly estimated using the MOST similarity functions which, however, are not directly applicable to problems at the scale of LES. On the other hand, subgrid eddy viscosity $K_{\text{m,sg}}$ and diffusivity (e.g., for heat) $K_{\text{h,sg}}$ can be estimated via the LES turbulence closure. For a 1.5-order TKE closure, for example, $K_{\text{m,sg}}$ is expressed as

$$K_{\text{m,sg}} = C_k l \sqrt{e}, \tag{9}$$

where e is the subgrid TKE, obtained by solving the TKE equation in the LES model, and C_k is an empirical parameter of about 0.15. The mixing length l is commonly set to the LES model grid resolution Δ. The subgrid eddy diffusivity can be expressed as

$$K_{\text{h,sg}} = K_{\text{m,sg}} P_r^{-1}, \tag{10}$$

where P_r is the Prandtl number, about 0.3.

The eddy diffusivity can be, in turn, used to estimate the aerodynamic resistance, e.g.,

$$r_{\text{h,sg}} = \int_{z_{0s}}^{z_1} K_{\text{h,sg}}^{-1}(z)\mathrm{d}z, \tag{11}$$

where z_{0s} is the aerodynamic roughness affected by the local characteristics of the land surface, and z_1 is the height of the lowest model layer. It is plausible to assume that

$$K_{\text{h,sg}}(z) = K_{\text{h,sg}}(z_1)\left(\frac{z}{z_1}\right)^n, \tag{12}$$

where $K_{\text{h,sg}}(z_1)$ is the subgrid eddy diffusivity at z_1. Then, for $n = 1$, we have

$$r_{\text{h,sg}} = \frac{z_1}{K_{\text{h,sg}}(z_1)} \ln\left(\frac{z_1}{z_{0s}}\right), \tag{13}$$

and for other n values,

$$r_{h,sg} = \frac{z_1}{(1-n)K_{h,sg}(z_1)}[1 - (\frac{z_1}{z_{0s}})^{n-1}],$$ (14)

For simplicity, we assume that $r_{h,sg} = r_{q,sg}$ in Eqs. (7) and (8), which are then used to compute subgrid surface fluxes.

2.2 MOST macroscopic constraint
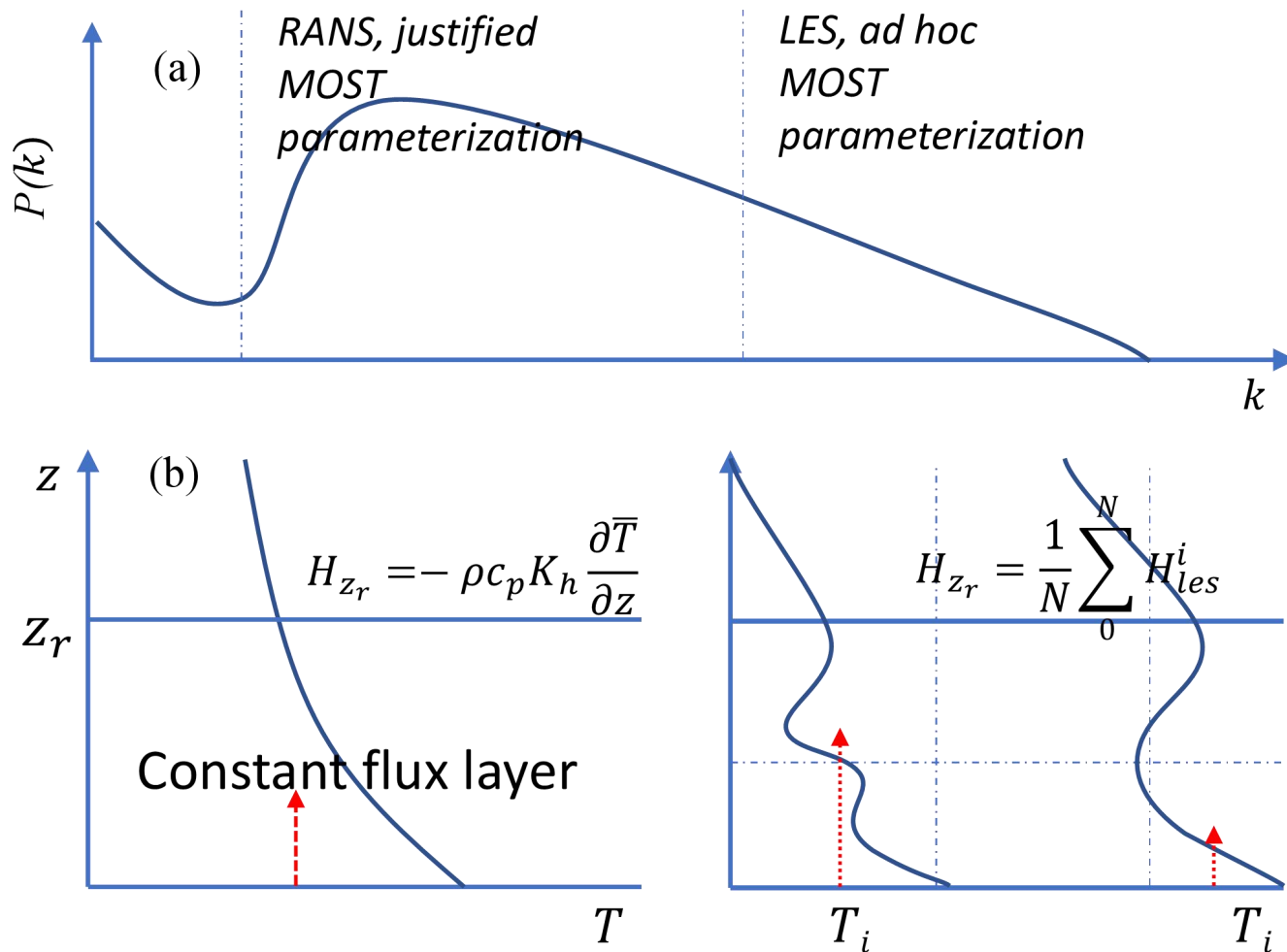
Figure 2. (**a**) Schematic energy spectrum of eddies, $P(k)$, as a function of wave number k; (**b**) Schematic profile of T in Reynolds-averaged Navier-Stokes (RANS) models (left) and LES models (right). z_r is the height of the constant flux layer.

Figure 2a shows the wavenumber ranges represented by RANS and LES models, while Fig. 2b visually demonstrates that the MOST parameterization, suitable for RANS models, may not hold true for LES models. In the constant flux layer, such as the sensible-heat flux and temperature profiles, the relationship can be well approximated with the MOST for RANS models, but deviates when applied to LES models (Sullivan et al., 1994). Utilizing MOST-based surface-flux parameterizations

125 contradicts the MOST assumptions and introduces internal inconsistencies within LES models, manifesting as disparities between MOST-based estimations of eddy viscosity and diffusivity and those derived from LES subgrid closure. However, if we compute surface fluxes locally as outlined in Section 2.1 and integrate the fluxes over a sufficiently large domain for which the MOST works well, then it is required that

$$\frac{1}{N}\sum_1^N H_{\text{les}}^i = H_{\text{most}} = -\rho c_p K_h \frac{\partial \overline{T}}{\partial z}, \tag{15}$$

130 where H_{les}^i is the surface sensible heat flux estimated by LES for grid cell i, N is the total number of grid cells in the domain, and $\overline{T}$ is the average temperature over the domain. Eq. (15) is not warranted if the fluxes are simply computed as stated in Section 2.1. Thus, a macroscopic constraint needs to be applied to the local surface flux estimates to ensure adherence to Eq. (15).

We use sensible heat flux for the discussion of the macroscopic constraint. A correction to H_{les}^i is made to ensure adherence

135 to Eq. (15), namely,

$$H_{\text{les,new}}^i = \mu H_{\text{les}}^i, \tag{16}$$

$$\mu = \frac{H_{\text{most}}}{\frac{1}{N}\sum_0^N H_{\text{les}}^i}, \tag{17}$$

where $H_{\text{les,new}}^i$ is the updated surface sensible heat flux. We apply the proposed MOST correction up to a height of 50 m. This correction indeed pertains to the constant flux layer. At the surface, vertical velocity $w_g^i = 0$, and H_{les}^i is entirely subgrid,

140 i.e.,

$$H_{\text{les}}^i = -\rho C_p K_{h,\text{sg}}^i \frac{\partial T_g^i}{\partial z}, \tag{18}$$

Hence, the macroscopic constraint becomes a constraint on the LES subgrid eddy diffusivity,

$$K_{h,\text{sg, new}}^i = \mu K_{h,\text{sg}}^i, \tag{19}$$

The same formulation applies to latent heat flux and momentum flux.

145 In practice, H_{most} can be estimated as follows. Suppose the LES domain consists of J land use types with σ_j being the fraction of land use type j. Then, H_{most} can be approximated using the mosaic approach (see Niu et al., 2011),

$$H_{\text{most}} = \sum_j \sigma_j H_j \tag{20}$$

and

$$H_j = -\alpha_j \rho C_p \frac{(\overline{T}_{a,j} - \overline{T}_{0,j})}{\overline{r}_{h,j}} \tag{21}$$

150 where $\overline{T}_{a,j}$, $\overline{T}_{0,j}$ and $\overline{r}_{h,j}$ are mean air temperature, mean surface temperature, and aerodynamic resistance for land use type j from LES domain, respectively. α_j represents the efficiency factor of H_{most} for land use type j. Further elucidation regarding the determination of these α values can be found in the Supplementary Material.

3 Description of experimental site and setup

3.1 Description of the observation site and data

155 We employed the multi-scale evapotranspiration flux observation datasets over heterogeneous land surfaces in the Heihe River Basin from HiWATER (Liu et al., 2011; Li et al., 2013). These datasets encompassed observations from various sites, including the Daman Site (38.85°N, 100.37°E, 1556.00 m ASL), Village Site (38.85°N, 100.35°E, 1561.87m ASL), Orchard Site (38.84°N, 100.36°E, 1559.63m ASL), and radiosonde sounding observations from the Zhangye National Climate Observatory (39.08°N, 100.27°E, 1556.06 m ASL) (Fig. 3). The Daman, Village, and Orchard Sites were situated within the

160 agricultural fields of the Daman Irrigation Area in Zhangye City, China, featuring maize fields, villages, and orchards as representative land surfaces, respectively. Several sensors recorded meteorological data at varying heights above the ground. Specifically, wind speed and wind direction sensors were installed at heights of 3, 5, 10, 15, 20, 30, and 40 m, all oriented northward. An air pressure sensor was situated 2 m above the ground. Additionally, a four-component radiometer was mounted at 12 m, facing south. Soil temperature probes were deployed at the soil surface (0 cm) and depths of 2, 4, 10, 20,

165 40, 80, 120, and 160 cm, all located 2 m south of the meteorological tower and oriented southward. Soil moisture sensors were buried at depths of 2, 4, 10, 20, 40, 80, 120, and 160 cm, all positioned 2 m south of the meteorological tower.

The eddy covariance (EC) system at the Daman site, Village site, and Orchard site were mounted at 4.5, 6.2, and 7.0 m, respectively, with all systems operating at a sampling frequency of 10 Hz. These systems were consistently oriented northward, and the distance between the sonic anemometer (CSAT3) and the CO_2/H_2O analyzer (Li7500A) was maintained

170 at 17, 20, and 0 cm, respectively. The collected EC data underwent rigorous preprocessing to ensure data quality. The EC data were initially temporally aggregated into 30-minute intervals to facilitate subsequent analysis. Furthermore, the quality of observational data underwent a classification process that stratified data quality into distinct levels based on criteria such as Δst (stationarity) and integral turbulent characteristics (ITC) using the methodology outlined by Foken and Wichura (1996). Only data within class 1 represented high-quality data ($\Delta st < 30$ and ITC < 30) were considered. A five-step data

175 quality control process was also implemented for the half-hourly flux data. These steps involved: eliminating data obtained during periods of sensor malfunction, characterized by anomalous diagnostic signals and automatic gain control values exceeding 65; rejecting data collected within 1 hour of precipitation events; discarding incomplete 30-minute data segments if missing data accounted for more than 3% of the raw 30-minute record; excluding data acquired during nighttime hours when the friction velocity (u_*) fell below 0.1 m s^{-1} (Blanken et al., 1998); considering only wind directions ranging from

180 315° to 0° and 0° to 45° to mitigate potential influences from adjacent EC sensors or environmental factors such as nearby brackets.
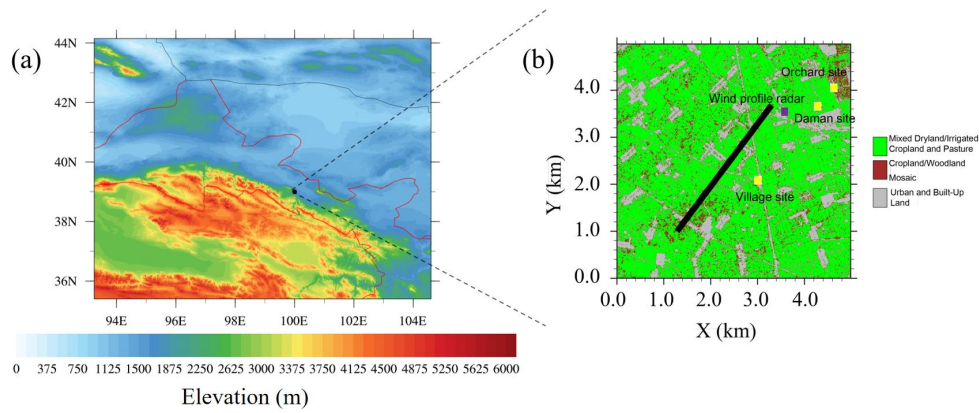
Figure 3. (**a**) The location of the observation site and (**b**) land use map. The black solid line is the optical length of a large aperture scintillometer (LAS).

3.2 Real experiment setup

The real experiments were conducted over a homogeneous surface, which includes three distinct land use types: "Mixed Dryland/Irrigated Cropland and Pasture" (hereafter MDICP) (represented by Daman site), "Urban and Built-up Land"(hereafter UBL) (represented by Village site) and "Cropland/woodland mosaic" (hereafter CWM) (represented by Orchard site) (Fig. 3b). The simulation domain was defined as $100 \times 100 \times 100$ grid points within a 5 km × 5 km area, extending to a depth of 2.6 km. Vertical discretization consisted of 100 layers with a resolution Δz stretching from 10 m to 40 m. The horizontal grid spacing was set at $\Delta x = \Delta y = 50$ m. A Rayleigh damping layer was implemented at a height of 500 m from the top to dampen the gravity waves. Initial profiles for horizontal wind speed, potential temperature, and humidity were extracted from soundings conducted at the Zhangye Station at 0800 local time (LT) on August 20, 2012 (Fig. 4). Solar shortwave radiation and upward longwave radiation fluxes observed at the Daman Station from 0800 to 1800 LT were used to force the model. Initial soil temperature and soil moisture conditions for MDICP, UBL, and CWM were derived from observations collected at 0800 LT on August 20, 2012, at the Daman, Village, and Orchard Stations, respectively. Each simulation spanned 10 hours, during which the weather conditions were sunny and free from any influence of weather systems. The choice of physics parameterization schemes was as follows: the 1.5-order TKE closure (Deardorff, 1980; Zhang et al., 2018) was selected for subgrid closure, while the revised MM5 Monin-Obukhov scheme (Jimenez, 2012) was employed for the surface layer. z_{0s} from different land use types were obtained from a lookup table. For MDICP, CWM, and UBL, α values of 0.94, 0.94, and 1.03 were assigned to sensible heat flux, while for latent heat flux, the values were 0.92, 0.92, and 1.09, respectively, based on the method in Supplementary Material.
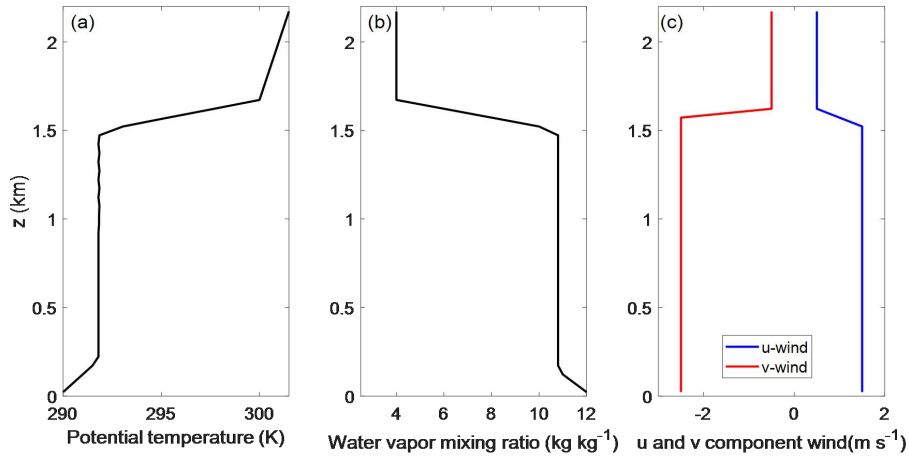
Figure 4. Initial (**a**) potential temperature, (**b**) water vapor mixing ratio, and (**c**) u, v components of wind speed, derived based on the soundings at the Zhangye Station (39.08°N, 100.27°E, 1556.06 m ASL) at 0800 local time (LT) on August 20, 2012.

We employed three distinct surface flux schemes to facilitate a comprehensive comparison. The new MOST-r scheme is evaluated alongside two other existing schemes: the Noah-MP land-surface scheme which incorporates MOST-based flux formulations coupled to LES (referred to as LES-Noah), and the local flux calculation scheme developed by Shao et al. (2013) (referred to as LES-S13). The observed sensible and latent heat flux, averaged from three EC sites, was employed as the benchmark for evaluating sensible and latent heat flux by LES. The simulated sensible and latent heat flux at a height of 10 m was juxtaposed with these observations for validation purposes.

Furthermore, the effects of varying horizontal grid resolutions on the MOST-r results were investigated by changing the model grid spacing $\Delta x = \Delta y$ from 100 to 10 m. Concomitant adjustments were made to the time steps to maintain numerical stability. The details of sensitivity experiments are listed in Table 1. The root mean square error (rmse) was used to measure the difference between different methods and ground-measured data:

$$\text{rmse} = [M^{-1} \sum (f^{\text{obs}} - f)^2]^{1/2}, \tag{22}$$

where M is the number of observations, f^{obs} are the fluxes measured by EC system, and f are the fluxes calculated by different methods.

Table 1. Lists of sensitivity experiments.

Case	EXP 1	EXP 2	EXP 3	EXP4
Scheme	MOST-r	MOST-r	MOST-r	MOST-r
Δx (m)	100	50	25	10
Case	EXP5	EXP6	EXP7	EXP8
Scheme	LES-S13	LES-S13	LES-S13	LES-S13
Δx (m)	100	50	25	10
Case	EXP9	EXP10	EXP11	EXP12

Scheme	LES-Noah	LES-Noah	LES-Noah	LES-Noah
Δx (m)	100	50	25	10

4 Results

4.1 Correction of MOST-r

225 We have conducted a comparative analysis involving MOST-r, LES-Noah, and LES-S13. To evaluate the correction of MOST-r for H and LE quantitatively, rmses for time- and domain- averaged H and LE between different experiments and observations are calculated and shown in Table 2. The estimated H and LE computed by MOST-r are closer to the observations than those by LES-Noah and LES-S13 methods. For example, when $\Delta x = 50\,\text{m}$, MOST-r has corrections of 22.7 W m^{-2} for H and 55.4 W m^{-2} for LE compared with LES-Noah. Similarly, compared to LES-S13, MOST-r has corrections of 24.0 W m^{-2} for H and 53.7 W m^{-2} for LE, respectively. In general, MOST-r consistently outperforms the other 230 two methods, with LES-S13 yielding the second-best results, while LES-Noah displays the least favorable outcomes.

Table 2. Rmse between different experiments and observations for time- and domain-averaged H and LE.

	Scheme	Δx = 100 m	Δx = 50 m	Δx = 25 m	Δx = 10 m
	LES-Noah	50.8	52.3	58.3	63.7
rmse(H) (W m^{-2})	LES-S13	51.3	53.6	56.3	60.0
	MOST-r	31.2	29.6	29.3	28.3
	LES-Noah	81.0	85.9	92.9	95.8
rmse(LE) (W m^{-2})	LES-S13	81.3	84.2	89.5	93.1
	MOST-r	31.6	30.5	30.8	29.9

4.2 Profiles of the time- and domain-averaged fluxes estimated by MOST-r

Profiles of the time- and domain-averaged sensible heat fluxes (H, H_g and H_{sg}) and latent heat fluxes (LE, LE_g and LE_{sg}), as estimated by LES-Noah, LES-S13, MOST-r, and observations, are shown in Figs. 5-6. H estimates derived from MOST-r are 235 generally closer to the measurements than those by LES-Noah and LES-S13 (Fig. 5a-c). Profiles of H estimated by LES-Noah, LES-S13, and MOST-r decrease with height linearly near the surface, extending until the inversion layer (Fig. 5d-f). This behavior is similar to the findings in Shao et al. (2013). In the bulk of the boundary layer, H is primarily attributed to H_g, with H_{sg} playing a negligible role. Close to the surface, H_{sg} takes precedence when turbulence occurs at finer scales. Similarly, LE estimates yielded by MOST-r are generally closer to the measurements than those by LES-Noah and LES-S13 240 (Fig. 6d-f). The near-surface flux estimated by MOST-r varies little with height, effectively meeting the assumptions associated with a constant flux layer. Our earlier analysis in Section 2.2 and reference to Eq. (15) reveal that the flux within the constant flux layer differs between RANS and LES. Traditional LES-Noah has failed to align with MOST, resulting in fluctuations in the constant flux layer as a function of height. LES-S13, devoid of MOST constraints, yields inferior results.

In this regard, MOST-r represents a significant improvement, with H_{sg} estimates generated by MOST-r surpassing those derived from LES-S13.
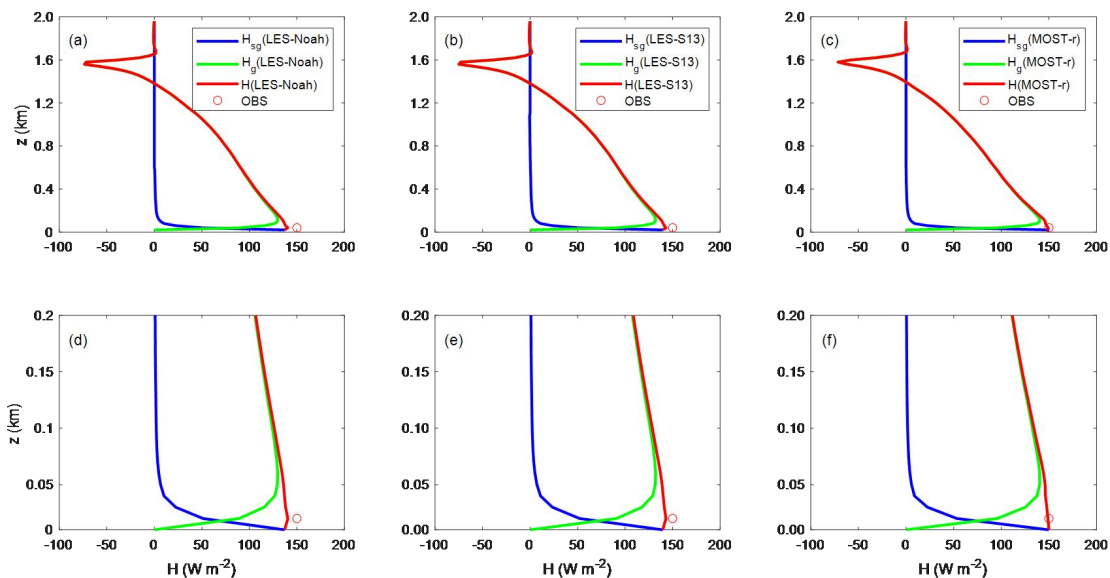
Figure 5. Profiles of H (red line), H_g (green line), and H_{sg} (blue line) estimated by (**a**) LES-Noah, (**b**) LES-S13, (**c**) MOST-r averaged over the model domain and during 1200 - 1300 LT. Profiles of H (red line), H_g (green line), and H_{sg} (blue line) estimated by (**d**) LES-Noah, (**e**) LES-S13, (**f**) MOST-r for the lower 200 m. The red circle is the averaged observation from three EC systems. The horizontal grid spacing is set to $\Delta x = 50$ m for the large-eddy simulations.
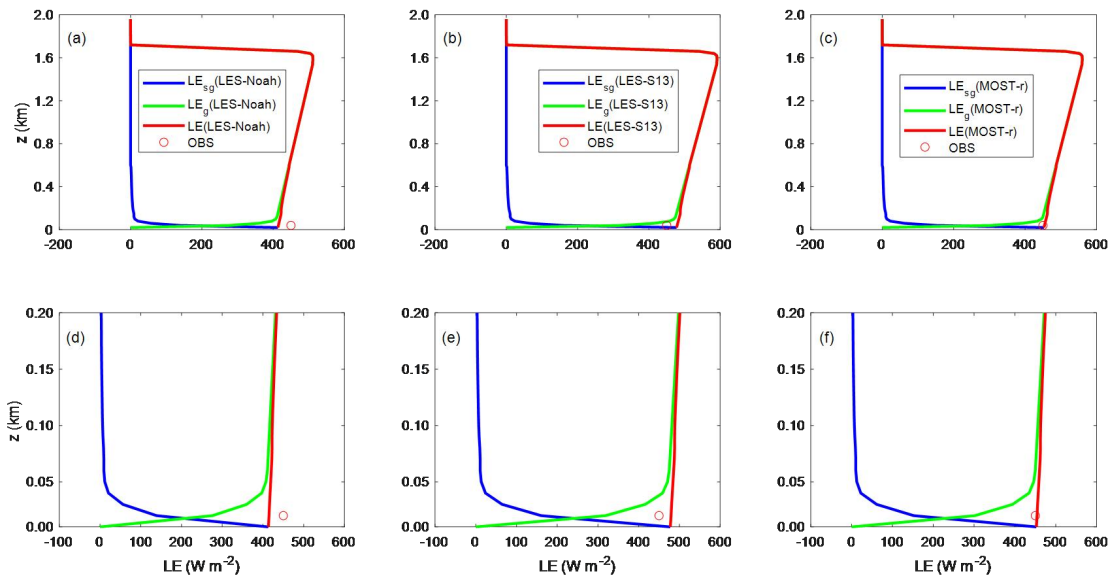
Figure 6. Similar to Fig. 5, but for latent heat flux.

4.3 Patterns of surface H and LE estimated by MOST-r

The study compares surface sensible heat (H) and latent heat (LE) flux patterns estimated by MOST-r, LES-Noah, and LES-
S13. All patterns were temporally averaged between 1200 and 1300 LT (Fig. 7a-c). The patterns of H and LE estimated by
MOST-r exhibit a striking similarity with those by LES-Noah and LES-S13. This parallelism indicates that MOST-r's
constraining influence over heterogeneous surface conditions effectively maintains the overall pattern of heat flux. This
phenomenon is intriguing and signifies the adaptability of MOST-r's constraints in accommodating varying surface
characteristics without fundamentally altering the heat flux pattern. Furthermore, the patterns of H and LE by MOST-r
demonstrate a concordance with the patterns of land use. For example, the UBL regions exhibit the highest H (> 300 W m^{-2})
estimated by MOST-r. Conversely, the H estimated by MOST-r over the MDICP and CWM is lower, hovering around 100
W m^{-2}. The maximum LE (> 500 W m^{-2}) is concentrated over the MDICP areas, whereas the LE over the UBL is much lower,
at around 200 W m^{-2}. In short, the H and LE patterns closely mirror the distinctive characteristics of the underlying land use.

The bilinear interpolation of grid point results from within the LES domain to approximate values at specific observation
points was used to allow for a direct comparison between estimations and observations. In particular, the focus is on areas
classified as MDICP and UBL. Over the MDICP and UBL, the estimated H and LE computed by MOST-r are closer to the
EC observations than those by LES-Noah and LES-S13 methods (Fig. 8). The investigation extends to several other critical
parameters, namely net radiation flux (R_{net}), surface skin temperature (T_s), and ground heat flux (G), where the estimations in
real-case scenarios are cross-referenced with measurements (Fig. 9). Over MDICP and UBL, the estimated R_{net} by MOST-r
are closer to the observations than those by LES-Noah and LES-S13. For example, the simulated R_{net} by MOST-r is up to 50
W m^{-2} higher than the observed values. In contrast, R_{net} by LES-S13 is more than 100 W m^{-2} higher than the observed values.
Furthermore, the R_{net} over UBL by all methods is smaller than that over MDICP. The assessment extends to surface skin
temperature (T_s), revealing that MOST-r achieves a notably superior agreement with observations over MDICP and UBL. In
contrast, LES-Noah and LES-S13 tend to overestimate T_s by up to 3 °C compared to observed values. Consistent with the
R_{net} findings, T_s is generally higher over UBL than MDICP across all methods. The G estimated by MOST-r matches the
observations and is better than that by LES-Noah and LES-S13 over MDICP and UBL. In contrast, LES-Noah tends to
overestimate G by up to 30 W m^{-2} over MDICP, further underscoring the proficiency of MOST-r. These findings affirm that
MOST-r consistently outperforms LES-Noah and LES-S13 in providing estimations that closely align with observations
across a spectrum of critical parameters.
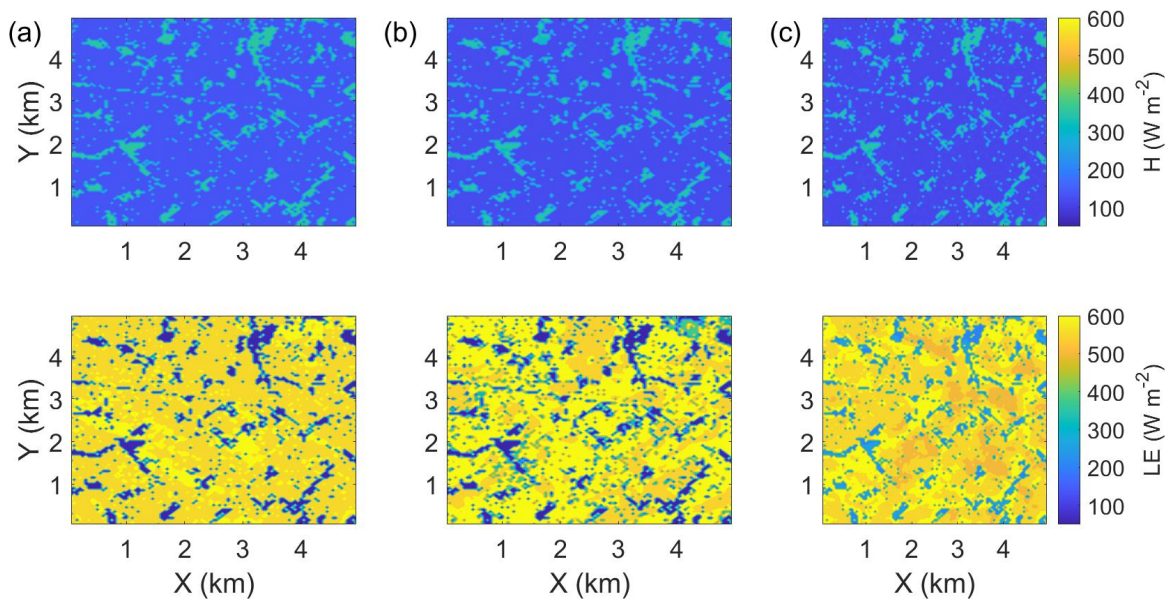
Figure 7. Patterns of surface sensible heat flux (*H*) and latent heat flux (*LE*) estimated by (**a**) LES-Noah, (**b**) LES-S13, (**c**) MOST-r averaged during 1200 - 1300 LT. The horizontal grid spacing is set to $\Delta x = 50$ m for the large-eddy simulations.
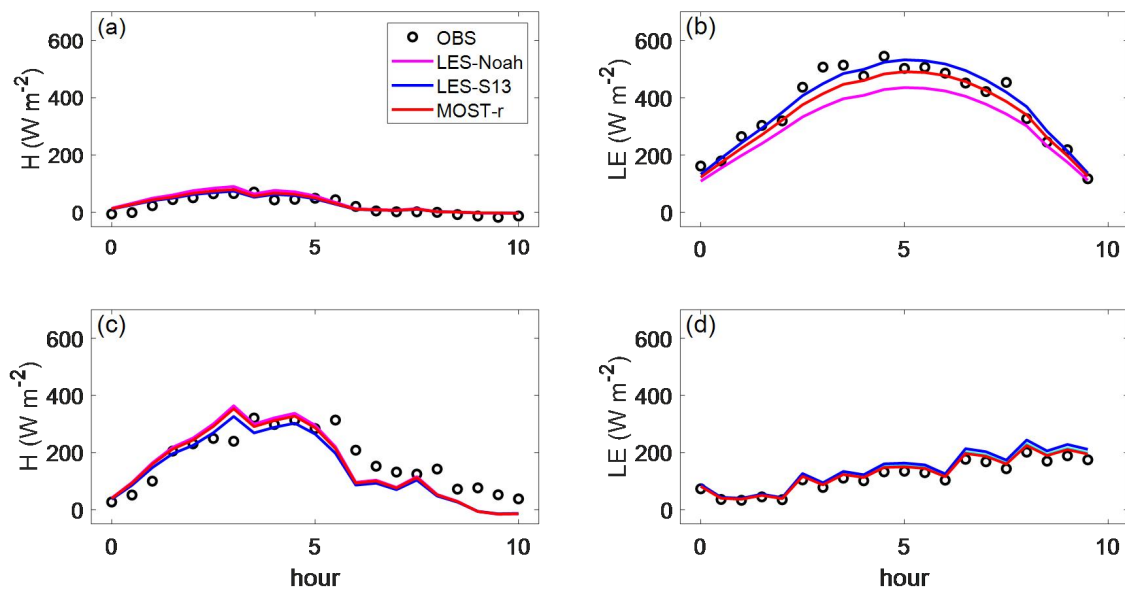
Figure 8. Time series of [(**a**) *H*, (**b**) *LE*] over MDICP and [(**c**) *H*, (**d**) *LE*] over UBL by observation, LES-Noah, LES-S13, and MOST-r method with $\Delta x = 50$ m.
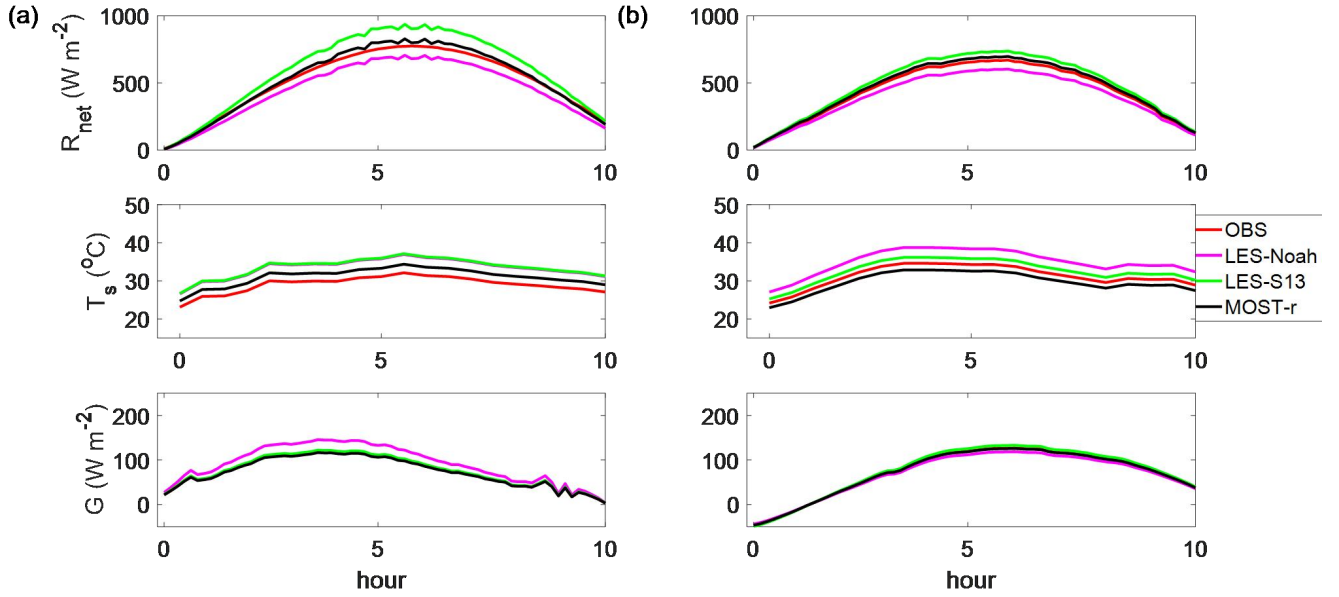
Figure 9. Net radiation flux (R_{net}), surface temperature (T_s), ground heat flux (G) estimated by LES-Noah, LES-S13, MOST-r, and observations over (**a**) MDICP and (**b**) UBL.

4.4 The effect of horizontal grid spacing on the correction by MOST-r

290   In pursue a comprehensive understanding of the impact of horizontal grid spacing (Δx) on the corrective capacity of MOST-r, a series of sensitivity experiments were conducted, systematically varying the horizontal grid spacing. The findings of these experiments are shown in Fig. 10 and Table 2. The corrective influence exerted by MOST-r on H and LE remains remarkably consistent as the horizontal grid spacing is progressively reduced (Fig. 10a-b). In contrast, surface H_{les} and LE_{les} estimated by LES-S13 decrease with Δx decrease, indicating that Δx has a large effect on surface H_{les} and LE_{les} by LES-S13.

295   These results are similar to those in Shin and Hong (2013), where the domain averaged subgrid fluxes decrease with the decrease of Δx, while the resolved fluxes increase. Consequently, it becomes evident that the MOST-r scheme maintains its corrective efficacy across varying horizontal grid spacings without exhibiting undue sensitivity to this parameter.

To delve into the impact of horizontal grid spacing (Δx) on the macroscopic constraint imposed by MOST, we present a comprehensive analysis of the μ parameter, as depicted in Fig. 10c. The results illustrate that the value of μ increases with Δx

300   decrease. Specifically, μ for H transitions from 1.00 at $\Delta x = 100$ m to 1.68 at $\Delta x = 25$ m, indicating that the macroscopic constraint of MOST on the LES increases with the decrease of horizontal grid spacing. In addition, μ for LE is smaller than that for H, indicating that the macroscopic constraint imposed by MOST on H is larger than that on LE (Fig. 10c).
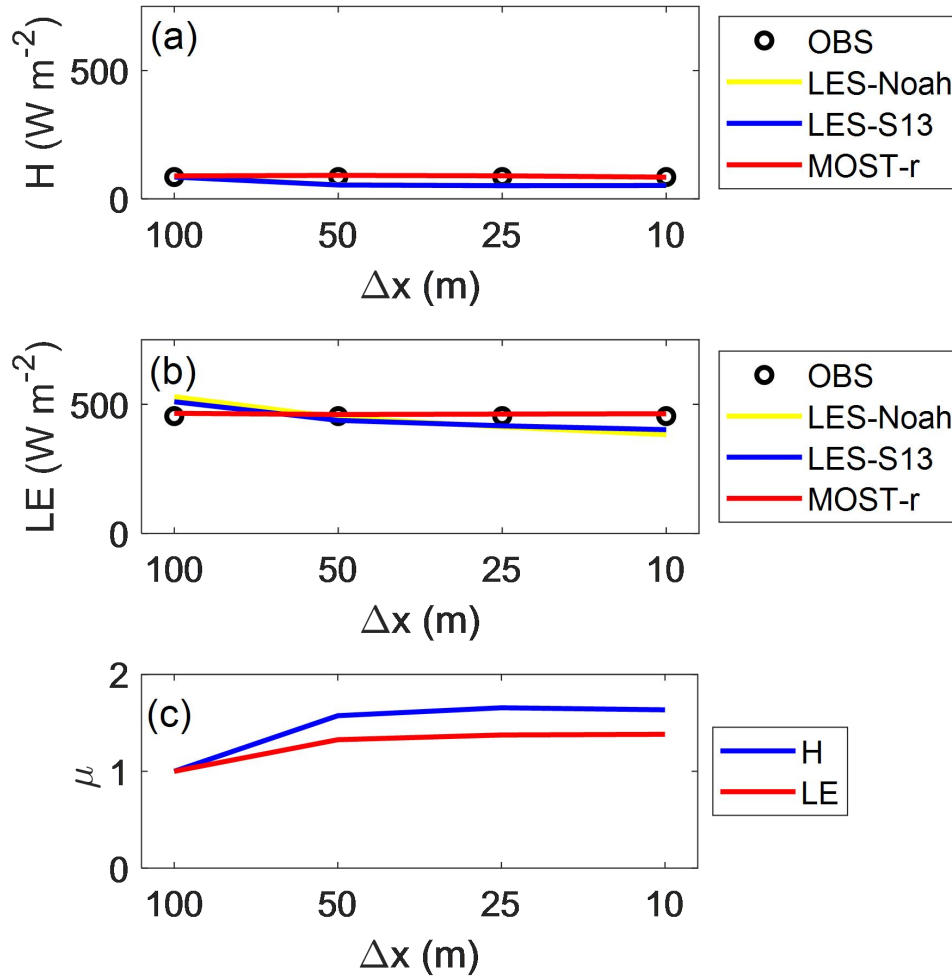
305 **Figure 10.** (**a**) *H* and (**b**) *LE* by observation, LES-Noah, LES-S13, and MOST-r averaged over the model domain and during 1200 - 1300 LT with different horizontal grid spacing ($\Delta x = 100, 50, 25, 10$ m). Variations of (**c**) μ for *H* and *LE* with different horizontal grid spacing ($\Delta x = 100, 50, 25, 10$m) averaged over the model domain and during 1200 - 1300 LT.

5 Conclusion and discussion

In response to the inconsistencies in using the MOST for parameterization of surface fluxes in LES models and the deficits
310 of the scheme proposed by Shao et al. (2013), we presented here the MOST-r scheme suitable for flux estimates of LES models. MOST-r consists of two components: first, it computes LES subgrid fluxes using eddy viscosity and diffusivity estimates from the LES closure tailored to local turbulence characteristics, and second, it incorporates a macroscopic

constraint, which aligns fluxes averaged over the LES domain with MOST principles, suitable for application in the surface layer.

315 We conducted a series of real-case experiments over an oasis surface in Northwestern China, employing the MOST-r scheme. Comparative analyses were performed, pitting the Noah-MP coupled with LES (LES-Noah) and the LSM in Shao et al. (2013) coupled with LES (LES-S13) against the new scheme. MOST-r consistently outperforms the other two methods, with LES-S13 yielding the second-best results, while LES-Noah displays somewhat less favorable outcomes. Traditional LES-Noah failed to adhere to MOST principles, causing flux discrepancies within the constant flux layer as a function of height.

320 On the other hand, LES-S13, lacking the MOST constraints, provided less accurate outcomes than the MOST-r scheme. MOST-r stands as a substantial improvement, with its ability to adhere to the MOST on large scales, particularly regarding the sensible heat flux estimates. It is noted that the MOST-r's constraining effect preserves the spatial patterns of the fluxes. This feature of the MOST-r scheme enables the LES model to correctly reproduce the spatially averaged fluxes while maintaining the flux patterns arising from surface heterogeneity. Our tests consistently demonstrate MOST-r's superiority

325 over LES-Noah and LES-S13, aligning closely with observational data across various key surface variables. Sensitivity experiments regarding horizontal resolution reveal that the MOST-r scheme produces grid-resolution invariant fluxes and thereby remedies the major deficit of the schemes directly based on the MOST, such as the LES-Noah scheme. We observed that the macroscopic constraint imposed by MOST on LES strengthens as the horizontal grid spacing decreases, with a greater influence on H than LE.

330 As previously mentioned, the two-part eddy viscosity model proposed by Sullivan et al. (1994) provided important insight into achieving alignment of subgrid closure with MOST across different spatial scales. But as far as flux estimates in LES models are concerned, the use of eddy viscosity and diffusivity derived from the LES turbulent closure accounts for the heterogeneities on scales larger than the LES model resolution. Hence, the MOST-r scheme already integrated the basic ideas of the two-part eddy viscosity model of Sullivan et al. (1994), without invoking the assumption of reduced turbulent

335 contribution to subgrid eddy viscosity and diffusivity. This enables the MOST-r scheme to better model the surface flux patterns. Instead of attempting to derive a general scale-invariant scheme for flux estimates, we provided a scheme that is both simple and effective for LES models.

While our findings have exhibited encouraging progress in aligning fluxes with MOST principles, the complexity and heterogeneity of surfaces introduce uncertainties and challenges in relation to our novel approach. Addressing this matter

340 may entail delving into the inertial sublayer, which could potentially extend beyond the initial grid points near the surface. Should we pursue this avenue in the future, a carefully devised strategy will be necessary to handle grid points within the viscous sublayer, where surface heterogeneity significantly influences outcomes.

Code availability. The source code used in this study is the WRF version 4.3 in the LES mode. WRF model can be

345 downloaded at https://www2.mmm.ucar.edu/wrf/users/download/get_sources.html (WRF Users page). The MOST-r scheme code can be accessed by contacting Bangjun Cao (caobj1989@163.com).

Data availability. The data presented in the paper can be accessed by contacting Bangjun Cao (caobj1989@163.com).

Author contributions. Shao and Cao had the original idea for the study. Cao and Yin conducted model simulation. Cao interpreted the data and plotted the figures. Cao wrote the article with contributions from all the co-authors. Project administration, Yang; funding acquisition, Yang; review and editing, Shao and Liu.

Competing interests. The contact author has declared that neither they nor their co-authors have any competing interests.

Acknowledgment. Thanks to the Heihe Watershed Allied Telemetry Experimental Research for the field observation data.

Financial support. This research has been supported by the National Natural Science Foundation of China (grant nos. 41975130, 42175174) and by the Second Tibetan Plateau Scientific Expedition and Research Program (STEP) (grant nos. 2019QZKK0102).

References

Blanken, P., Black, T., Neumann, H., Hartog, C., Yang, P., Nesic, Z., Staebler, R., Chen,W., Novak, M. : Turbulence flux measurements above and below the overstory of a boreal aspen forest. Boundary-Layer Meteorol, 89, 109-140, https://doi.org/10.1023/A:1001557022310, 1998.

Deardorff, J.: Efficient prediction of ground surface temperature and moisture with inclusion of a layer of vegetation. J. Geophys. Res., 83, 1889–1903, https://doi.org/10.1029/JC083iC04p01889, 1978.

Deardorff, J.: Stratocumulus-capped mixed layers derived from a three-dimensional model. Bound.-Lay. Meteorol., 18, 495–527, https://doi.org/10.1007/BF00119502, 1980.

Foken, T., Wichura, B.: Tools for quality assessment of surface based flux measurements. Agric. For. Meteorol, 78, 83-105, https://doi.org/10.1016/0168-1923(95)02248-1, 1996.

Holt, T., and S. Raman.: A review and comparative evaluation of multilevel boundary layer parameterizations for first-order and turbulent kinetic energy closure schemes. Reviews of Geophysics, 26 (4), 761-80, https://doi.org/10.1029/RG026i004p00761,1988.

Huang, H., Margulis, S.: Evaluation of a fully coupled large-eddy simulation-land surface model and its diagnosis of land-atmosphere feedbacks. Water Resource Research, 46, W06512, https://doi.org/10.1029/2009WR008232, 2010.

Jimenez, P., and J. Dudhia: Improving the representation of resolved and unresolved topographic effects on surface wind in the WRF model. J. Appl. Meteor. Climatol., 51, 300–316, https://doi.org/10.1175/JAMC-D-11-084.1, 2012.

Li, X., Cheng, G., Liu, S., Xiao, Q., Ma, M., Jin, R., Che, T., Liu, Q., Wang, W., Qi, Yuan., Wen, J., Li, H., Zhu, G., Guo, J., Ran, Y., Wang, S., Zhu, Z., Zhou, J., Hu, X., and Xu, Z.: Heihe watershed allied telemetry experimental research (HiWATER): scientific objectives and experimental design. Bulletin of the American Meteorological Society, 94, 1145–1160, https://doi.org/10.1175/BAMS-D-12-00154.1, 2013.

Redelsperger, J. L., F. Mahe, and P. Carlotti.: A Simple and General Subgrid Model Suitable Both for Surface Layer and

380   Free-Stream Turbulence. Boundary-Layer Meteorology, 101 (3), 375–408, https://doi.org/10.1023/A:1019206001292, 2001.

Liu, S. M., Xu, Z. W., Wang, W. Z., Jia, Z. Z., Zhu, M. J., Bai, J., and Wang, J. M.: A comparison of eddy-covariance and large aperture scintillometer measurements with respect to the energy balance closure problem, Hydrol. Earth Syst. Sci., 15, 1291–1306, https://doi.org/10.5194/hess-15-1291-2011, 2011.

Liu, S., Xu, Z., Zhu, Z., Jia, Z., Zhu, M.: Measurements of evapotranspiration from eddy-covariance systems and large

385   aperture scintillometers in the Hai River Basin, China. Journal of Hydrology, 487, 24-33, doi: http://dx.doi.org/10.1016/j.jhydrol.2013.02.025, 2013.

Maronga, B., Raasch, S.: Large-eddy simulations of surface heterogeneity effects on the convective boundary layer during the LITFASS-2003 experiment. Bound.-Lay. Meteorol., 146, 17−44, https://doi.org/10.1007/s10546-012-9748-z, 2013.

Moeng, C.: A large-eddy simulation model for the study of planetary boundary-layer turbulence. J. Atmos. Sci., 41, 2052–

390   2062, https://doi.org/10.1175/1520-0469(1984)041<2052:ALESMF>2.0.CO;2, 1984.

Monin, A., Obukhov, A.: Basic laws of turbulent mixing in the ground layer of the atmosphere (in Russian). Tr Geofiz Inst Akad Nauk SSSR, 151, 163–187, 1954.

Niu, G., Yang, Z., Mitchell, K., Chen, F., Ek, M., Barlarge, M., Kumar, A., Manning, K., Niyogi, D., Rosero., E., Tewari, M., Xia, Y.: The community Noah land surface model with multiparameterization options (Noah-MP): Model description and

395   evaluation with local-scale measurements. J. Geophys. Res., 116, D12109, https://doi.org/10.1029/2010JD015139, 2011.

Oleson, K., Niu, G., Yang, Z., Lawrence, D., Thornton, P., Lawrence, P., Stockli, R., Dickinson, R., Bonan, G., Levis, S.: CLM3.5 Documentation. UCAR, http://cgd.ucar.edu/tss/clm/distribution/clm3.5, 2007.

Patton, E., Sullivan, P., Moeng, C.: The influence of idealized heterogeneity on wet and dry planetary boundary layers coupled to the land surface. J. Atmos. Sci., 62, 2078–2097, https://doi.org/10.1175/JAS3465.1, 2005.

400   Shao, Y., Liu, S., Schween, J., Schween, J., Crewell, S.: Large-eddy atmosphere-land-surface modeling over heterogeneity surfaces: model development and comparison with measurements. Bound.-Lay. Meteorol., 148, 333–356, doi: 10.1007/ s10546-013-9823-0, 2013.

Shin, H., Hong, S.,: Analysis of resolved and parameterized vertical transports in convective boundary layers at gray-zone resolutions. J. Atmos. Sci., 70, 3248–3261, https://doi.org/10.1175/JAS-D-12-0290.1, 2013.

405   Smagorinsky, J.: General circulation experiments with the primitive equations, Part I: the basic experiment. Mon. Wea. Rev., 91, 99–164, https://doi.org/10.1175/1520-0493(1963)091<0099:GCEWTP>2.3.CO;2, 1963.

Sullivan, P., J. C. Mcwilliams, and C. Moeng.: A subgrid-scale model for large-eddy simulation of planetary boundary-layer flows. Boundary-Layer Meteorology, 71(3), 247–76, https://doi.org/10.1007/BF00713741,1994.

Zhang, X., Bao, J., Chen, B., Grell, E.: A three-dimensional scale-adaptive turbulent kinetic energy scheme in the WRF-

410   ARW model. Mon. Wea. Rev., 146, 2023-2045, https://doi.org/10.1175/MWR-D-17-0356.1, 2018.